

Boosting room temperature magneto-ionics in Co₃O₄

Julius de Rojas¹, Alberto Quintana², Aitor Lopeandía¹, Joaquín Salguero³, José L. Costa-Krämer³, Llibertat Abad⁴, Maciej O. Liedke⁵, Maik Butterling⁵, Andreas Wagner⁵, Lowie Henderick⁶, Jolien Dendooven⁶, Christophe Detavernier⁶, Jordi Sort^{1,7*} & Enric Menéndez^{1*}

¹Departament de Física, Universitat Autònoma de Barcelona, E-08193 Cerdanyola del Vallès, Spain

²Department of Physics, Georgetown University, Washington, D.C. 20057, United States

³IMN-Instituto de Micro y Nanotecnología (CNM-CSIC), Isaac Newton 8, PTM, 28760 Tres Cantos, Madrid, Spain

⁴Institut de Microelectrònica de Barcelona, IMB-CNM (CSIC), Campus UAB, E-08193 Bellaterra, Spain

⁵Institute of Radiation Physics, Helmholtz-Center Dresden-Rossendorf, Dresden 01328, Germany

⁶Department of Solid State Sciences, CoCooN, Ghent University, Krijgslaan 281/S1, 9000 Ghent, Belgium

⁷Institució Catalana de Recerca i Estudis Avançats (ICREA), Pg. Lluís Companys 23, E-08010 Barcelona, Spain

*email: jordi.sort@uab.cat (J. Sort), enric.menendez@uab.cat (E. Menéndez)

Abstract

Voltage control of magnetism through electric field-induced oxygen motion (magneto-ionics) could represent a significant breakthrough in the pursuit for new strategies to enhance energy efficiency in a large variety of magnetic devices, such as magnetic micro-electro-mechanical systems (MEMS), magnetic logics, spin electronics, or neuromorphic computing, *i.e.*, envisaging ultra-low power emulation of the biological synapse. Boosting the induced changes in magnetization, magneto-ionic motion and cyclability (endurance) continue to be key challenges to turn magneto-ionic phenomena into real applications. Here, we demonstrate that, without degrading cyclability, room temperature magneto-ionic motion in electrolyte-gated paramagnetic and fairly thick (> 100 nm) Co₃O₄ films largely depends on the configuration used to apply the electric field. In particular, magneto-ionic effects are significantly increased both in terms of generated magnetization (6 times larger: from **118.5** to **699.2 emu cm⁻³**) and speed (35 times faster: from **33.1** to **1170.8 emu cm⁻³ h⁻¹**) if the electric field is applied across a conducting buffer layer (grown underneath the Co₃O₄ films), instead of directly contacting Co₃O₄. This is attributed to a greater uniformity and strength of the applied electric field when using the conducting layer. These results may trigger the use of oxygen magneto-ionics into promising new technologies, such as magnetic MEMS or brain-inspired computing, which require endurance and moderate speeds of operation.

Current computers rely on Von Neumann's structural design in which the central processing unit and memory constitute different sub-devices bridged by the communication bus. This is not only detrimental to data processing speed but also to energy efficiency, making the search for new computing architectures central for future information technologies¹⁻⁶. Neuromorphic computing relies on the use of devices that emulate the electrical behavior of the biological synapse, which is the memory and learning element of the brain, and has emerged as an alternative, which could render low-power information storage/processing^{2-4,6}. Intense research is currently being carried out in the use of electronic^{2,3} and spintronic-based^{4,5} approaches to mimic synapse's activity. However, these strategies are ultimately based on the use of electric currents (to generate magnetic fields through electromagnetic induction or spin-polarized electric currents via spin-transfer torque), involving a significant energy loss by heat dissipation through Joule effect^{7,8}. Voltage control of magnetism (VCM), wherein magnetism is controlled via an applied electric field in place of an electric current, could potentially represent a significant breakthrough, envisaging ultra-low power emulation of the biological synapse⁵. Besides its potential use in memories and computation, magnetoelectric materials have also shown potential, in recent years, to be used in magnetic micro-electro-mechanical systems, such as biomagnetic sensors⁹ or nanofluidics¹⁰, where effects induced at moderate rates (*e.g.*, 1 s) are appealing to boost energy efficiency.

VCM has conventionally branched into three broad approaches, including (i) single-phase, multiferroic materials¹¹, (ii) inverse magnetostriction effects in piezoelectric/ferromagnetic heterostructures^{12,13}, and (iii) surface charge accumulation in ferromagnetic metals (*i.e.*, direct electric field effect)^{14,15}. Each of the aforementioned VCM mechanisms has some drawbacks: multiferroics are limited in number, particularly at room temperature; strain-mediated heterostructures suffer from mechanical fatigue; and, in metals and alloys, electronic charging is only observed in ultra-thin ferromagnetic films.

Electric field-induced oxygen motion in magnetic materials (magneto-ionics) has recently revolutionized VCM since this mechanism may allow for a voltage-driven modulation of magnetic properties, such as coercivity, exchange bias field or magnetic anisotropy, to a level never reached by any other magnetoelectric means (*i.e.*, approaches (i), (ii) and (iii) above)^{6,16-28}. Magneto-ionics, with magnetoelectric coupling efficiencies of the order of 10^3 fJ/(V·m), deals so far with the lowest writing/retrieving energies ($\sim 10^{-3}$ fJ/bit = 1 aJ/bit) to write/delete a bit (*i.e.*, information unit)^{16,22}. This represents energies two and five orders of magnitude lower than those required in complementary metal oxide semiconductor (CMOS) technology ($\sim 10^{-1}$ fJ/bit) and magnetic-based devices like magneto-resistive random access memories or hard disk drives ($\sim 10^2$ fJ/bit), respectively²².

Typically, magneto-ionic systems consist of layered heterostructures in a condenser-like configuration to apply voltage in solid state. Ferromagnetic metals, such as Co¹⁶ or Fe²², are the target materials grown adjacent to GdO_x or HfO₂ layers, which act as ion reservoirs and, thereby, accepting or donating oxygen ions depending on the voltage polarity. Room temperature ionic motion is slow, involving times between 10^2 - 10^3 s (10^{-2} - 10^{-3} Hz in

frequency rate) to switch the magnetic state, such as the magnetic anisotropy easy axis from out-of-plane to in-plane and *vice versa* in ultra-thin Co layers by voltage-driven oxygen migration from a GdO_x reservoir¹⁶. Therefore, alongside the applied voltage, these solid electrolytes usually require of high temperatures since ion migration is a thermally activated process^{16–18,23,24}. In these magneto-ionic systems, the pristine ferromagnetic layer suffers from pronounced structural and compositional changes, leading to irreversibility¹⁷ and, thus, poor cyclability¹⁶. Recently, via a proton-based approach, excellent endurance and 10⁻¹ s (10 Hz) room temperature operation has been shown feasible in spite of certain instability since hydrogen retention is limited²³. An alternative approach is the use of structural oxygen (self-contained in the magnetic material of interest), hence avoiding the need of external oxygen sources²⁰. This has been shown in electrolyte-gated paramagnetic Co₃O₄ films, in which room temperature voltage-controlled on-off ferromagnetism has been achieved by electric switching of the oxidation state of cobalt (*i.e.*, voltage-driven reduction/oxidation), taking advantage of the defect-assisted voltage-driven migration of structural oxygen²⁰. Even though this route still yields slow room temperature magneto-ionic motion, it shows outstanding stability and promising cyclability since the target is already oxidized.

Herein, by applying electric field using a conducting rather than an insulating buffer layer underneath the Co₃O₄ films (like previously reported results)²⁰, we demonstrate that, without degrading cyclability, room temperature magneto-ionic motion in electrolyte-gated, paramagnetic and fairly thick Co₃O₄ films (thicknesses above 100 nm) can be enhanced in terms of both generated magnetization (6 times larger) and speed (35 times faster). This is ascribed to a greater uniformity and strength of the applied electric field achieved when using the conducting buffer layer as working electrode instead of directly contacting the Co₃O₄ film. Our results, showing the importance of properly optimizing device design to apply electric field, could promote the use of oxygen magneto-ionics for brain-inspired computing^{20,29} and new types of MEMS devices, which demand endurance and moderate speed of operation³⁰.

Results

Figs. 1a and 1b show the two types of film structures (Co₃O₄ (130 nm)/SiO₂ (20 nm)/[100]-oriented Si substrate and Co₃O₄ (130 nm)/TiN (170 nm)/[100]-oriented Si substrate, respectively) investigated in this work, aimed at unraveling the role of electric properties of the buffer layer underneath (*i.e.*, insulating for SiO₂ and conducting for TiN³¹: insulating vs. conducting configuration) in the magneto-ionic response of Co₃O₄.

Electrolyte-gating is used to apply voltage while performing in-plane vibrating sample magnetometry (VSM) –*i.e.*, magnetoelectric measurements–. A Pt wire is used as counter electrode, whereas the Co₃O₄ itself and the TiN are used as working electrodes for the Co₃O₄ (130 nm)/SiO₂ (20 nm)/substrate and Co₃O₄ (130 nm)/TiN (170 nm)/substrate sample configurations, respectively (see Methods for further details). The as-prepared Co₃O₄ samples (under no applied voltage) show virtually no ferromagnetic behavior in either the

insulating (Fig. 1c) or the conducting configuration (Fig. 1d), in agreement with their paramagnetic nature at room temperature²⁰. To investigate magneto-ionics in each configuration, the samples were subjected to -50 V for several hours and magnetic hysteresis loops of 25 min of duration were continuously recorded. After subjecting each sample to -50 V for 25 min (*i.e.*, upon the first hysteresis loop is recorded), the measurements show a clear hysteretic behavior, evidencing the emergence of ferromagnetism. The conducting configuration shows a remarkable increase in magnetization upon sweeping the first quadrant of the first hysteresis cycle, which doubles once the measurement reaches the fourth quadrant of the first loop. A much more gradual increase of the magnetization is observed in the insulating configuration. Fig. 1e shows the saturation magnetization (M_S) as a function of time (see Supplementary Figure 1 for further details on M_S quantification). The magnetic moment scales monotonically with time for each configuration, but with a 6-fold larger increase between SiO₂ and TiN in the total magnetization (**118.5 to 699.2 emu cm⁻³**, respectively) reached after magneto-ionic motion has stabilized. Furthermore, the time scale for ferromagnetism generation (“on” state) in the conducting configuration is significantly faster than in the insulating configuration. To compare properly the rate of “on” switching, this magnetization increase is determined by a linear fit of the M_S vs. t plot evaluated during the first 36 min of voltage application (wherein M_S in the TiN configuration fully saturates). The rates are **33.1 and 1170.8 emu cm⁻³ h⁻¹**, showing that the use of a conducting buffer layer enhances ion migration by a factor 35 with respect to the insulating buffer layer.

Looking at the M (magnetization)- H (applied magnetic field) loops (Figs. 1c and 1d), there are also marked shape differences. The conducting configuration exhibits more square-shaped and more tilted cycles (*i.e.*, it has a more “easy axis” character) than the insulating configuration. To examine the shape of the M - H loops, the squareness, defined as the ratio between the remnant magnetization (M_R) and M_S (M_R/M_S), and the slope of the hysteresis loop at the coercive field (H_C) normalized to M_S ($dM/dH (H = H_C) M_S^{-1}$) have been calculated for both the descending and ascending branches of the measured hysteresis loops (Fig. 1f). The conducting configuration exhibits higher M_R/M_S ratios and slopes at H_C throughout the time the voltage was applied, in concordance with more square-shaped and more tilted loops (*i.e.*, narrower distribution of coercive fields)³².

To further examine the nature of the electric field experienced by the Co₃O₄ samples, COMSOL simulations were performed to model the initial voltage distributions for each configuration upon electrolyte-gating (see Methods for further simulation details). In Figs. 1g and 1h, electric contact to the working electrodes (Co₃O₄ and TiN for the insulating and conducting configurations, respectively) is made at the top of the left plane which represents the samples, whereas the right plane corresponds to the counter electrode (*i.e.*, Pt wire).

Clear differences can be seen in the equipotential lines for the insulating (Fig. 1g) and conducting (Fig. 1h) configurations. In the insulating configuration, the dielectric nature of

SiO₂ and limited electric conductivity of Co₃O₄³³ manifest in a non-homogeneous voltage distribution along the vertical extent of the Co₃O₄ film, showing a weaker and less uniform applied electric field as the distance from the electric contact is increased. Conversely, in the other configuration, the conducting nature of TiN results in a nearly uniform voltage distribution along the vertical cross-section of the sample, which gives rise to a larger and better defined electric field along the direction perpendicular to the Co₃O₄ film plane. In contrast to the dielectric configuration, the whole Co₃O₄ film is activated for magneto-ionic motion (see Supplementary Figure 2).

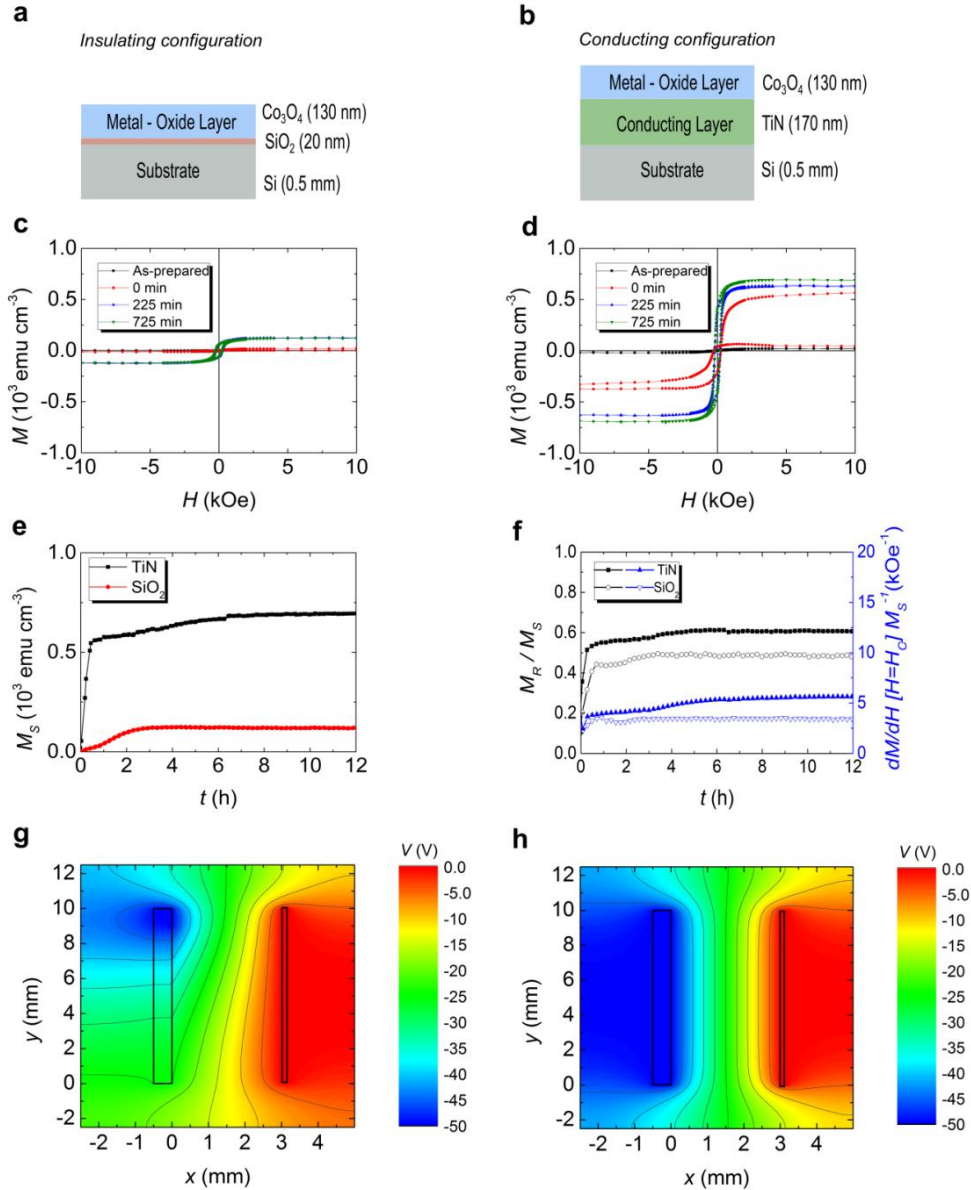


Fig. 1 Sample configurations: (a) Co₃O₄ on SiO₂ (insulating configuration) and (b) Co₃O₄ on TiN (conducting configuration). (c) and (d) consecutive hysteresis loops under -50 V gating for the insulating and conducting configurations, respectively, taken by in-plane vibrating sample magnetometry. (e) Time evolution of the saturation magnetization (M_s vs. t) and (f) squareness (M_R/M_S) & slope of hysteresis loop at H_c normalized to M_s for each configuration. (g) and (h) show the COMSOL simulations of the initial voltage distribution at the moment in which the insulating and the conducting configurations, respectively, are electrolyte-gated (equipotential lines are drawn).

To assess the degree of structural and compositional change that Co_3O_4 undergoes with voltage for the two investigated configurations, cross-section lamellae of the pristine and treated Co_3O_4 films were prepared and characterized by high-angle annular dark-field scanning transmission electron microscopy (HAADF-STEM) and electron energy loss spectroscopy (EELS), respectively (Fig. 2).

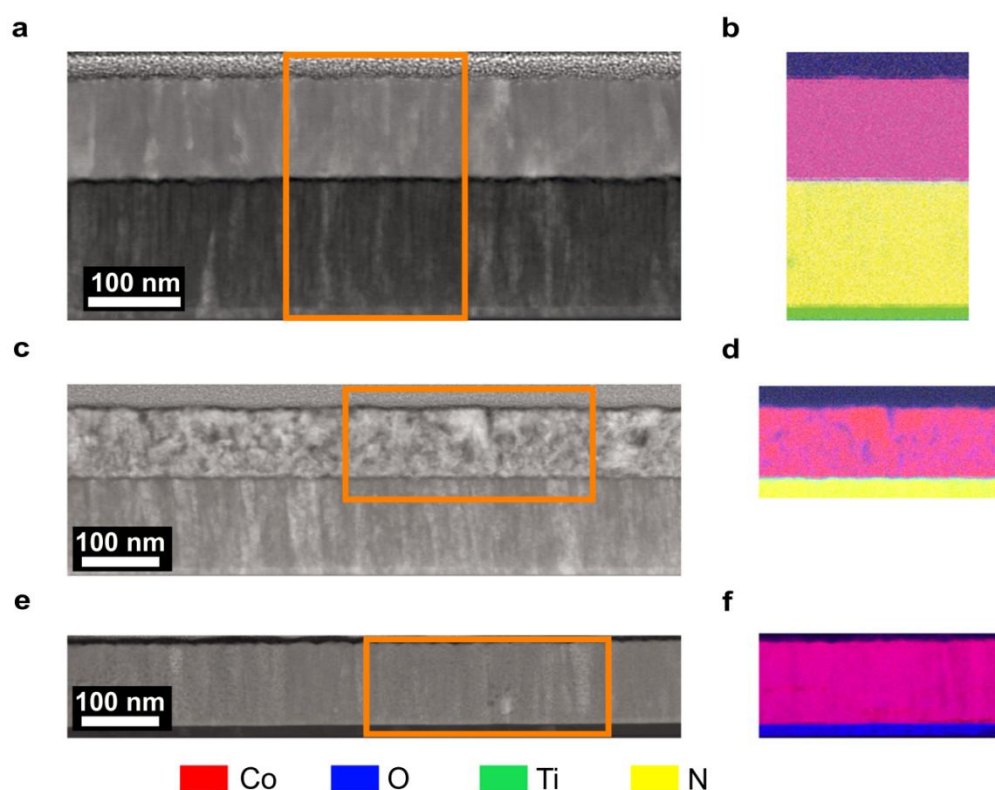


Fig. 2 Structural and compositional characterization by high-angle annular dark-field scanning transmission electron microscopy (HAADF-STEM) and electron energy loss spectroscopy (EELS), respectively. (a–b), (c–d), and (e–f) are HAADF-STEM images and elemental EELS mappings of the areas marked in orange corresponding to pristine $\text{Co}_3\text{O}_4/\text{TiN}$, $\text{Co}_3\text{O}_4/\text{TiN}$ negatively biased at -50 V for 80 min, and $\text{Co}_3\text{O}_4/\text{SiO}_2$ also negatively biased -50 V for 80 min, respectively. Colors corresponding to each element for the EELS analyses are depicted at the bottom of the figure.

The morphology of the pristine sample grown on TiN (Fig. 2a) shows regular, columnar-shaped grains as it happens in Co_3O_4 deposited by atomic layer deposition on SiO_2 ²⁰. This morphology remains rather unaltered after treating the Co_3O_4 film deposited on SiO_2 with -50 V for 80 min (Fig. 2e). On the contrary, the Co_3O_4 morphology in the conducting configuration treated at -50 V for 80 min shows no columnar grains consistent with a more nanostructured Co_3O_4 phase (Fig. 2c and Supplementary Figure 3).

To locally quantify the Co/O distribution, Co and O EELS mappings were conducted for the as-grown films and the samples treated at -50 V for 80 min for both insulating and conducting configurations (Fig. 2). Co (red) and O (blue) are homogeneously distributed in the as-grown sample with conducting configuration (Fig. 2b) and nearly homogeneously distributed in the treated sample with the insulating configuration (Fig. 2f), which sharply

contrasts with the sample treated under -50 V in the conducting configuration (Fig. 2d). The corresponding Co (red) and O (blue) EELS mappings reveal the presence of Co-rich and O-rich areas due to voltage-driven ion migration. In contrast to the sample grown on SiO_2 , electrolyte-gating of the Co_3O_4 sample grown on TiN results in O_2 bubbling, evidencing that, on top of oxygen redistribution within the film²⁰, oxygen is also released into the liquid medium, which acts as an oxygen sink.

Further structural characterization was carried out by $\theta/2\theta$ X-ray diffraction (XRD), high resolution transmission electron microscopy (HRTEM) and variable energy positron annihilation spectroscopy (VEPAS). The XRD patterns of the as-prepared samples are consistent with a textured Co_3O_4 phase along (1 1 1), (2 2 2) and (3 1 1) planes. Upon electrolyte-gating at -50 V for 80 min, the intensity of the (1 1 1) and (2 2 2) planes strongly decreases while that of the (3 1 1) planes reduces only slightly. For the Co_3O_4 sample grown on TiN, the peak corresponding to (1 1 1) planes fully vanishes after the application of this negative voltage (Fig. 3a). Furthermore, as seen in the detailed XRD view of Fig. 3b, the conducting configuration shows the emergence of a new peak after gating at -50 V for 80 min, which is consistent with the diffraction from (0 0 2) planes of hexagonal close-packed Co (HCP-Co).

Moreover, high resolution transmission electron microscopy (HRTEM) was performed in the cross-section of a Co_3O_4 film grown on TiN and treated at -50 V (Fig. 3c). The inset shows the fast Fourier transform of the area marked with a red rectangle, which results in three well-defined spots highlighted in red circles and numbered 1, 2 and 3. The corresponding interplanar distances are 1.991, 1.920 and 2.535 Å, respectively. The interplanar distance of 1.920 Å is unambiguously ascribed to (1 0 1) HCP-Co (ICDD JCPDF 00-005-0727), whereas 1.991 Å could be associated with either (0 0 2) HCP-Co or (4 0 0) Co_3O_4 (ICDD JCPDF 00-009-0418). However, since the as-prepared Co_3O_4 films do not exhibit traces of (4 0 0) planes and (0 0 2) HCP-Co is observed by XRD, the interplanar distance of 1.991 Å is likely to belong to HCP-Co. Finally, 2.535 Å is consistent with an O-deficient (3 1 1) Co_3O_4 (ICDD JCPDF 00-009-0418) phase²⁰.

To examine the microstructure of the as-prepared films at atomic level, variable energy positron annihilation spectroscopy (VEPAS) was performed (Fig. 3d). Both low and high electron momentum fraction (S and W , respectively) as a function of positron implantation energy, E_p , virtually overlap up to the first 50 nm in depth. The differences at further depths of the film are essentially due to the different chemical nature of the buffer layer. This indicates that the as-prepared films grown on both substrates have similar amount and type of defects, independently of the substrate they are grown on.

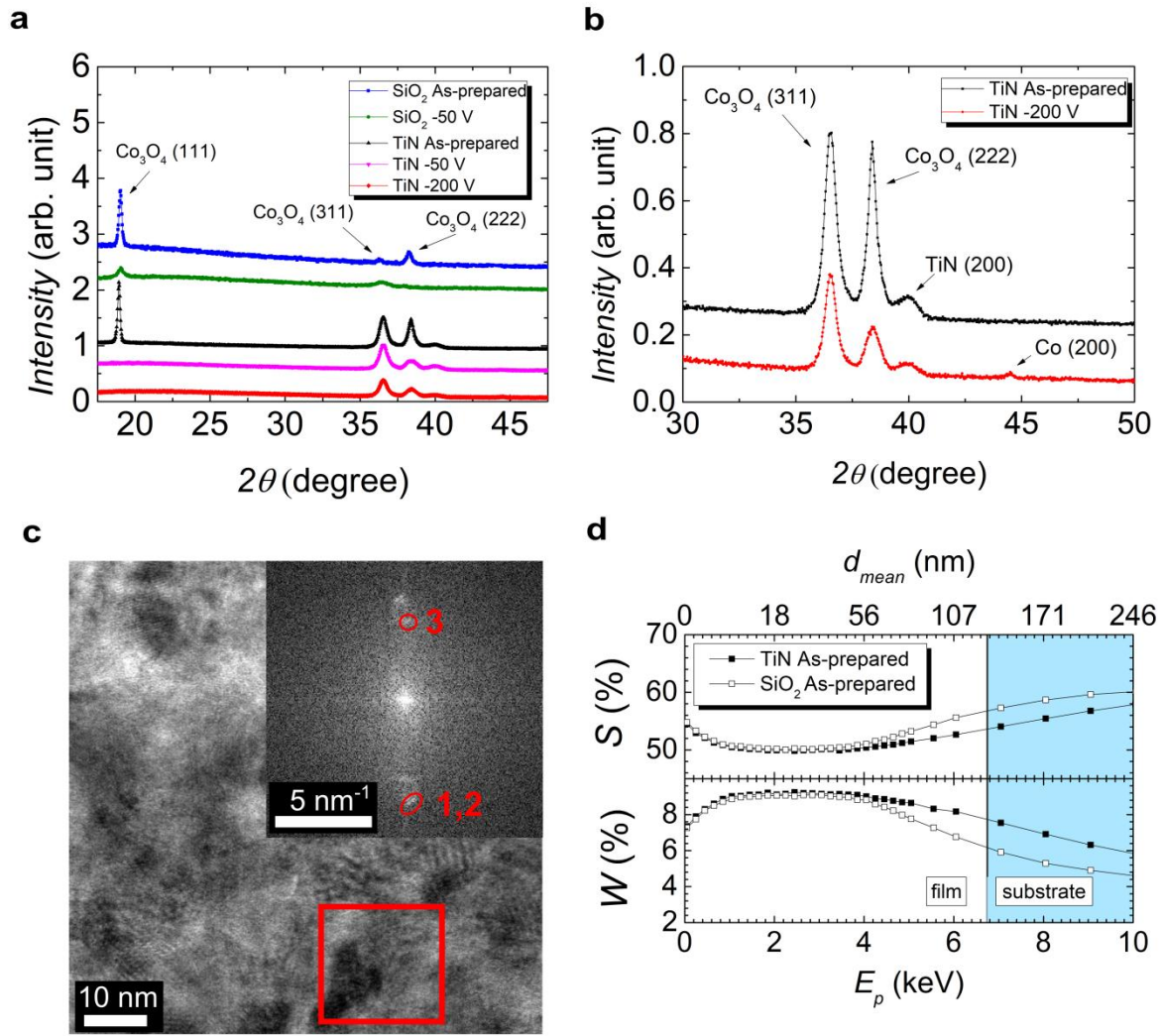


Fig. 3 Structural characterization by $\theta/2\theta$ -X-ray diffraction (XRD), high resolution transmission electron microscopy (HRTEM) and variable energy positron annihilation spectroscopy (VEPAS). (a) $\theta/2\theta$ -XRD diffraction patterns of the as-prepared and treated samples at -50 V, and at -200 V for the Co_3O_4 grown on TiN. (b) Detailed view of the XRD patterns corresponding to the Co_3O_4 grown on TiN. (c) HRTEM image of the cross-section of a Co_3O_4 film grown on TiN and treated at -50 V. The inset shows the fast Fourier transform of the area marked with a red rectangle. (d) Low and high electron momentum fraction (S and W , respectively) as a function of positron implantation energy, E_p , for the as-prepared samples. " d_{mean} " stands for average depth.

The onset voltage for magneto-ionic motion and cyclability has also been investigated for both configurations (Fig. 4). To determine the onset voltage, the gating was monotonically decreased in steps of -2 V to observe when the system started to display ferromagnetic behavior. Afterwards, the voltage polarity was reversed to test the cyclability of the magneto-ionic effect. The Co_3O_4 film grown on TiN exhibits an onset voltage of -4 V and requires of +50 V to fully recover the pristine paramagnetic state. Conversely, the insulating configuration shows an onset voltage of -10 V and requires of +10 V to recover the initial state, in agreement with previously reported results on the same configuration but with a thicker SiO_2 buffer layer²⁰.

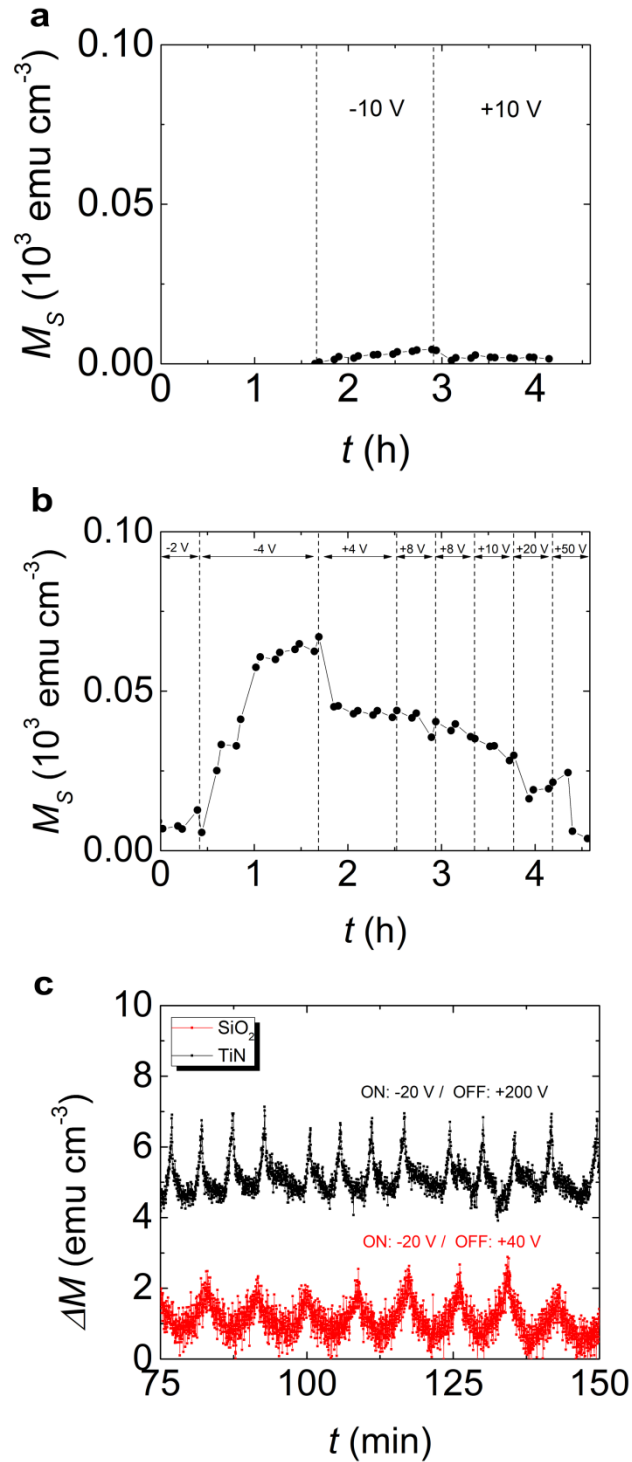


Fig. 4 (a) and (b) onset/recovery behavior of the insulating and conducting configurations, respectively. (c) Cyclability for both sample configurations ($-20 \text{ V}/+40 \text{ V}$ and $-20 \text{ V}/+200 \text{ V}$ pulses for the insulating and conducting configurations, respectively).

While the onset/recovery process is repeatable, to perform cyclability tests the applied biases were increased in order to enhance the magneto-ionic signal-to-noise ratio and, thus, better observe endurance. 30 cycles were performed using voltage pulses of $-20 \text{ V}/+40 \text{ V}$ and $-20 \text{ V}/+200 \text{ V}$ for the insulating and conducting configurations, respectively (Fig. 4c). The

change in magnetization relative to the background magnetization is observed to be repeatable in time scale and magnetization quality, suggesting suitable reproducibility for long term use.

Discussion

The role of the electric properties of the buffer layer (*i.e.*, insulating SiO₂ or conducting TiN) in the magneto-ionic behavior of Co₃O₄ thin films has been investigated. As seen in Fig. 1, upon electrolyte-gating at –50 V, the use of a conducting rather than an insulating buffer layer boosts magneto-ionics in terms of both long-term generated magnetization (6-fold relative increase: from **118.5** to **699.2 emu cm⁻³**) and initial magneto-ionic motion (35 times faster: from **33.1** and **1170.8 emu cm⁻³ h⁻¹**).

These different behaviors are already revealed by the *M-H* hysteresis loops which show pronounced differences in shape. The conducting configuration results in more square-shaped loops with larger squareness and more tilted branches (*i.e.*, narrower distribution of coercive fields and, thus, higher slopes at H_C), evidencing a more “easy-axis” nature than the insulating configuration. This is consistent with the generation of more uniform ferromagnetic regions in the Co₃O₄ film (with better defined shape anisotropy) when a conducting buffer layer is used, in agreement with the COMSOL simulations of Figs. 1g and 1h. In the insulating configuration, the interplay between the dielectric nature of SiO₂ and the limited electric conductivity of Co₃O₄ manifests in a non-homogeneous voltage distribution along the Co₃O₄ film, showing a weaker and less uniform applied electric field as the distance from the electric contact increases. Conversely, in the other configuration, the conducting nature of TiN results in a nearly uniform voltage distribution along the vertical cross-section of the sample, which gives rise to a larger and better defined electric field along the direction perpendicular to the Co₃O₄ film plane. In contrast to the dielectric configuration, the Co₃O₄ film on TiN is fully and homogeneously activated alongside its complete vertical extent. This results in a well-defined path with a nearly full perpendicular electric field component for magneto-ionic motion in the conducting configuration. On the contrary, in the insulating configuration, due to the presence of a vertical component caused by the limited electric conductivity of Co₃O₄, the strength and speed of magneto-ionic motion is hindered. This is in concordance with a broader size distribution of ferromagnetic regions in the electrolyte-gated Co₃O₄ film on SiO₂, in agreement with the magnetometry results which indicate lower squareness values and less tilted branches (*i.e.*, broader distribution of coercive fields). This is also evidenced by the evolution of coercivity with time for the consecutive loops taken while electrolyte-gating both configurations at –50 V (Supplementary Figure 4). Whereas the insulating configuration results in a monotonic increase of H_C with time, the conducting configuration shows a maximum at the very beginning. This maximal behavior resembles the typical dependence of coercivity with particle size in magnetic systems, consistent with a scenario in which a more homogeneous generation of ferromagnetic regions occurs, uniformly evolving in size, likely starting from a

superparamagnetic behavior, followed by a single domain state (maximum of H_C) and ending with a multi-domain configuration³².

The effect of configuration on the compositional and structural properties of Co_3O_4 is clearly observed in Fig. 2. The morphology of the pristine samples shows regular, columnar-shaped grains (Fig. 2a and Supplementary Figure 3) and homogeneous composition (Fig. 2b). This largely remains upon treating the Co_3O_4 film deposited on SiO_2 with -50 V for 80 min (Figs. 2e and 2f). Conversely, the morphology of the conducting configuration treated at -50 V for 80 min shows almost no columnar grains and a highly nanostructured Co_3O_4 phase (Fig. 2c and Supplementary Figure 3) with Co and O segregation (Fig. 2d). This indicates that the conducting configuration can electrically modulate ion migration at much higher strengths. This is further confirmed by XRD and HRTEM which show traces of metallic Co only for the conducting configuration (Fig. 3). Even though the as-prepared Co_3O_4 films show similar crystallographic features regardless buffer layer, further structural characterization to examine the local microstructure of the as-prepared samples was carried out by VEPAS. As can be seen in Fig. 3d, both low and high electron momentum fraction (S and W , respectively) as a function of positron implantation energy, E_p , virtually overlap, indicating that Co_3O_4 either grown on SiO_2 or TiN exhibits analogous defect environment, ruling out minor microstructure differences in Co_3O_4 as the origin of the observed magneto-ionic effects. Nevertheless, voltage-driven ion diffusion seems to be facilitated along $(1\ 1\ 1)$ planes as evidenced by the strong decrease in intensity of the $(1\ 1\ 1)$ and $(2\ 2\ 2)$ planes, with the $(1\ 1\ 1)$ planes fully vanishing for the Co_3O_4 sample grown on TiN (Fig. 3a).

As seen in Fig. 4, the minimum voltage bias required to perform an onset/recovery cycle is asymmetric for the Co_3O_4 film grown on TiN (-4 V/ $+50$ V), while it is symmetric for the Co_3O_4 film grown on SiO_2 (-10 V/ $+10$ V). The onset bias is significantly larger for the conducting configuration (-4 V (conducting TiN) vs. -10 V (insulating SiO_2)). In contrast to the insulating configuration, the use of a conducting buffer layer activates the whole Co_3O_4 sample, resulting in a more intense and better defined perpendicular electric field and, thus, in enhanced magneto-ionic effect and motion. O_2 bubbling is noticeably observable only in the conducting configuration, evidencing that, on top of oxygen redistribution²⁰, oxygen is released into the liquid electrolyte, which acts as an oxygen sink, and as an oxygen reservoir due to the oxygen solubility in propylene carbonate. The voltage asymmetry in the conducting configuration can be linked to O_2 bubbling since propylene carbonate reaches O supersaturation and the oxygen forming bubbles cannot be recovered.

Cycling (Fig. 4) further corroborates the faster magneto-ionic rates of the conducting configuration, particularly during the generation of the “on” states. Time span in the insulating configuration has been enlarged to reach a suitable signal-to-noise ratio, as a consequence of the slower magneto-ionic kinetics. For the conducting configuration, cyclability is lost when lower voltages (higher in absolute value but negatively biased) are applied (e.g., -50 V) due to strong irreversible O_2 bubbling.

In summary, we have investigated the role of the electric properties of the substrate in the magneto-ionic behavior of Co_3O_4 thin films. Polycrystalline 130 nm-thick Co_3O_4 films have been grown by atomic layer deposition on either insulating SiO_2 or conducting TiN buffer layers. The use of a conducting rather than contacting from the top Co_3O_4 (when deposited onto an insulating substrate) boosts magneto-ionics in terms of both generated magnetization (6-fold increase: from **118.5** ($\text{Co}_3\text{O}_4/\text{SiO}_2$) to **699.2 emu cm⁻³** ($\text{Co}_3\text{O}_4/\text{TiN}$)) and magneto-ionic rates (35 times faster: from **33.1** ($\text{Co}_3\text{O}_4/\text{SiO}_2$) to **1170.8 emu cm⁻³ h⁻¹** ($\text{Co}_3\text{O}_4/\text{TiN}$)). Upon gating, transmission electron microscopy and electron energy loss spectroscopy show the emergence of Co-rich areas at a greater intensity for the Co_3O_4 grown on a conducting substrate. Magnetization measurements also show a marked increase in the squareness ratio and a decrease in the switching field distribution of the hysteresis loops from Co_3O_4 deposited on the conducting layer, evidencing the generation of more uniform ferromagnetic regions. This dissimilar behavior between the use of either an insulating or a conducting substrate arises from the intensity and uniformity of the electric field, which are maximized when using a conducting substrate while preserving stability and endurance. These results demonstrate the importance of the specific device design (and, in particular, the use of conducting substrates to apply electric field in electrolyte-gated oxide materials) in order to optimize the strength and speed of the magneto-ionic effect. Our results prompt the way to make oxygen magneto-ionics feasible for practical applications in fields like neuromorphic and stochastic computing or magnetic MEMS, where high frequencies are not necessarily required for device engineering²⁹.

Methods

Sample preparation

130 nm thick Co_3O_4 films were grown on two substrates: i) thermally oxidized non-doped Si wafers (SiO_2 (20 nm)/[1 0 0]-oriented Si (0.5 mm)), and ii) non-doped Si wafers coated with a TiN buffer layer (TiN (170 nm)/[1 0 0]-oriented Si (0.5 mm)). Deposition was carried out by plasma enhanced atomic layer deposition as described in references 20, 33 and 34.

Magnetoelectric characterization

Magnetic measurements under electrolyte gating (*i.e.*, magnetoelectric characterization) were carried out at room temperature in a vibrating sample magnetometer from Micro Sense (LOT-Quantum Design), with a maximum applied magnetic field of 2 T. The sample was mounted in a homemade electrolytic cell filled with anhydrous propylene carbonate with Na^+ solvated species (5 - 25 ppm), and the magnetic properties were measured along the film plane after applying different voltages, using an external Agilent B2902A power supply, between the sample and the counter-electrode in a similar fashion of that presented in references 15, 20 and 28. The Na^+ solvated species in the electrolyte are aimed at reacting with any traces of water¹⁵. The magnetic signal was normalized to the area of the sample exposed to the electrolyte during the voltage application process. All hysteresis loops were background-corrected and the correction was carried out at high fields (*i.e.*, fields always far above saturation fields) to eliminate linear contributions (paramagnetic and diamagnetic signals).

Structural and compositional measurements

$\theta/2\theta$ X-ray diffraction (XRD) patterns were recorded on a Philips X'Pert Powder diffractometer with a PIXcel^{1D} detector using Cu K_α radiation.

High resolution transmission electron microscopy (HRTEM), high-angle annular dark-field scanning transmission electron microscopy (HAADF-STEM) and electron energy loss spectroscopy (EELS) were performed on a TECNAI F20 HRTEM /STEM microscope operated at 200 kV. Cross sectional lamellae were prepared by focused ion beam and placed onto a Cu transmission electron microscopy grid.

Variable energy positron annihilation spectroscopy (VEPAS)^{35,36} was used to investigate depth-resolved open volume defects at the Slow-Positron System of Rossendorf (SPONSOR) beamline, which provides monoenergetic but variable energy positron beam.

Modelling

A simulation of the charge distribution in each of the two systems was performed using COMSOL finite element analysis software. Estimation of the charge distribution considered charge conservation ($\nabla J = 0$), Ohm's law ($J = \sigma E$), and Gauss' law ($E = -\nabla V$). The geometry of the system was modeled in 2D to minimize computational needs. The geometry includes the silicon substrate (0.5 mm), the sample film (Co_3O_4 and buffer layer: either SiO_2 or TiN), contact layer (In solder onto Cu wire), a platinum counter electrode, all set in an electrochemical chamber filled with propylene carbonate. The sample film has been unified

to enable a tetragonal adaptive mesh within the computer memory resources. The effective electric conductivity (*i.e.*, electric conductance) has been modeled by weighing the different sub-layer constituting within the sample stack and normalizing relative to the thicknesses of each layer in the model. In the insulating configuration the silicon substrate is considered coated with a SiO₂ layer, electrically isolated from the sample. The sample essentially consists of a 130 nm Co₃O₄ layer on top the substrate. A value of electrical conductivity of 20 S/m for Co₃O₄ has been measured via a 4-probe van der Pauw measurement, in agreement with values from the literature³³.

The electrical conductivity for TiN was taken from literature, 3×10^5 S/m³¹. In the conducting configuration, the 170 nm of TiN and the 130 nm of Co₃O₄ are taken in combination. The large electrical conductivity of the TiN dominates the effective electrical conductivity of the sample section. Simulations shown are calculated for the system under –50 V gating voltage.

Data availability

The data used in this paper are available from the corresponding authors upon request.

References

1. Patterson, D. A. & Hennessy, J. L. in *Computer Organization and Design: The Hardware/Software Interface* (5th edition, Elsevier Inc., Amsterdam, 2014).
2. An, H., Bai K. & Yi, Y. The roadmap to realize memristive three-dimensional neuromorphic computing system. in *Advances in Memristor Neural Networks - Modeling and Applications* (ed. Ciufudean, C.) 25–44 (IntechOpen, 2018).
3. Xia, Q. & Yang, J. J. Memristive crossbar arrays for brain-inspired computing. *Nat. Mater.* **18**, 309–323 (2019).
4. Torrejon, J. et al. Neuromorphic computing with nanoscale spintronic oscillators. *Nature* **547**, 428–431 (2017).
5. Manipatruni, S., Nikonov, D. E. & Young, I. A. Beyond CMOS computing with spin and polarization. *Nat. Phys.* **14**, 338–343 (2018).
6. Mishra, R., Kumar, D. & Yang, H. Oxygen-migration-based spintronic device emulating a biological synapse. *Phys. Rev. Appl.* **11**, 054065 (2019).
7. Shiota, Y. et al. Induction of coherent magnetization switching in a few atomic layers of FeCo using voltage pulses. *Nat. Mater.* **11**, 39–43 (2012).
8. Song, C. et al. Recent progress in voltage control of magnetism: materials, mechanisms, and performance. *Prog. Mater. Sci.* **87**, 33–82 (2017).
9. Marauska, S., Jahns, R., Greve, H., Quandt, E., Knöchel, R. & Wagner, B. MEMS magnetic field sensor based on magnetoelectric composites. *J. Micromech. Microeng.* **22**, 065024 (2012).

10. Duschek, K., Uhlemann, M., Schlörb, H., Nielsch, K. & Leistner, K. Electrochemical and in situ magnetic study of iron/iron oxide films oxidized and reduced in KOH solution for magneto-ionic switching. *Electrochem. Commun.* **72**, 153–156 (2016).
11. Eerenstein, W., Mathur, N. D. & Scott, J. F. Multiferroic and magnetoelectric materials. *Nature* **442**, 759–765 (2006).
12. Wang, Y., Hu, J., Lin, Y. & Nan C.-W. Multiferroic magnetoelectric composite nanostructures. *NPG Asia Mater.* **2**, 61–68 (2010).
13. Li, P. et al. Spatially resolved ferroelectric domain-switching-controlled magnetism in $\text{Co}_{40}\text{Fe}_{40}\text{B}_{20}/\text{Pb}(\text{Mg}_{1/3}\text{Nb}_{2/3})_{0.7}\text{Ti}_{0.3}\text{O}_3$ multiferroic heterostructure. *ACS Appl. Mater. Interfaces* **9**, 2642–2649 (2017).
14. Weisheit, M. et al. Electric field-induced modification of magnetism in thin-film ferromagnets. *Science* **315**, 349–351 (2007).
15. Quintana, A. et al. Voltage-induced coercivity reduction in nanoporous alloy films: a boost toward energy-efficient magnetic actuation. *Adv. Funct. Mater.* **27**, 1701904 (2017).
16. Bauer, U. et al. Magneto-ionic control of interfacial magnetism. *Nat. Mater.* **14**, 174–181 (2015).
17. Gilbert, D. A. et al. Structural and magnetic depth profiles of magneto-ionic heterostructures beyond the interface limit. *Nat. Commun.* **7**, 12264 (2016).
18. Gilbert, D. A. et al. Controllable positive exchange bias via redox-driven oxygen migration. *Nat. Commun.* **7**, 11050 (2016).
19. Baldrati, L., Tan, A. J., Mann, M., Bertacco, R. & Beach, G. S. D. Magneto-ionic effect in CoFeB thin films with in-plane and perpendicular-to-plane magnetic anisotropy. *Appl. Phys. Lett.* **110**, 012404 (2017).
20. Quintana, A. et al. Voltage-controlled ON-OFF ferromagnetism at room temperature in a single metal oxide film. *ACS Nano* **12**, 10291–10300 (2018).
21. Navarro-Senent, C. et al. Large magnetoelectric effects in electrodeposited nanoporous microdisks driven by effective surface charging and magneto-ionics. *ACS Appl. Mater. Interfaces* **10**, 44897–44905 (2018).
22. Ibrahim, F., Hallal, A., Dieny, B. & Chshiev, M. Establishing characteristic behavior of voltage control of magnetic anisotropy by ionic migration. *Phys. Rev. B* **98**, 214441 (2018).
23. Tan, A. J. et al. Magneto-ionic control of magnetism using a solid-state proton pump. *Nat. Mater.* **18**, 35–41 (2019).
24. Tan, A. J. et al. Hydration of gadolinium oxide (GdO_x) and its effect on voltage-induced Co oxidation in a Pt/Co/GdO_x/Au heterostructure. *Phys. Rev. Lett.* **3**, 064408 (2019).
25. Molinari, A., Hahn, H. & Kruk, R. Voltage-control of magnetism in all-solid-state and solid/liquid magnetoelectric composites. *Adv. Mater.* **31**, 1806662 (2019).
26. Robbenolt, S. et al. Electric field control of magnetism in iron oxide nanoporous thin films. *ACS Appl. Mater. Interfaces* **11**, 37338–37346 (2019)

27. Robbenolt, S. et al. Reversible, electric-field induced magneto-ionic control of magnetism in mesoporous cobalt ferrite thin films. *Sci. Rep.* **9**, 10804 (2019)
28. Navarro-Senent, C., Quintana, A., Menéndez, E., Pellicer, E. & Sort, J. Electrolyte-gated magnetoelectric actuation: phenomenology, materials, mechanisms and prospective applications. *APL Mater.* **7**, 030701 (2019)
29. Leighton, C. et al. Electrolyte-based ionic control of functional oxides. *Nat. Mater.* **18**, 13–18 (2019).
30. Harris, J. J., Jolivet, R. & Attwell, D. Synaptic energy use and supply. *Neuron* **75**, 762–777 (2012).
31. Jin, Y., Kim, Y.-G., Kim, J. H. & Kim, D. K. Electrical properties of DC sputtered titanium nitride films with different processing conditions and substrates. *J. Korean Ceram. Soc.* **42**, 455–460 (2005).
32. Leslie-Pelecky, D. L. & Rieke, R. D. Magnetic properties of nanostructured materials. *Chem. Mater.* **8**, 1770–1783 (1996).
33. Donders, M. E., Knoops, H. C. M., van de Sanden, M. C. M., Kessels, W. M. M. & Notten, P. H. L. Remote plasma atomic layer deposition of Co₃O₄ thin films. *J. Electrochem. Soc.* **158**, G92–G96 (2011).
34. Dendooven, J., Deduytsche, D., Musschoot, J., Vanmeirhaeghe, R. L. & Detavernier, D. Conformality of Al₂O₃ and AlN deposited by plasma-enhanced atomic layer deposition. *J. Electrochem. Soc.* **157**, G111–G116 (2010).
35. Anwand, W., Brauer, G., Butterling, M., Kissener, H. R. & Wagner A. Design and construction of a slow positron beam for solid and surface investigations. *Defect Diffus. Forum.* **331**, 25–40 (2012).
36. Krause-Rehberg, R. & Leipner, H. in *Positron Annihilation in Semiconductors* (Springer, Berlin, 1999).

Acknowledgements

Financial support by the European Research Council (SPIN-PORICS 2014-Consolidator Grant, Agreement N^o 648454), the Spanish Government (MAT2017-86357-C3-1-R and associated FEDER) and the Generalitat de Catalunya (2017-SGR-292 and 2018-LLAV-00032) is acknowledged. This work was partially supported by the Impulse-und Net-working fund of the Helmholtz Association (FKZ VH-VI-442 Memriox), and the Helmholtz Energy Materials Characterization Platform (03ET7015).

Author contributions

E.M. had the original idea and led the investigation. **J.d.R.**, **J.S.** and **E.M.** designed the experiments. **L.H.**, **J.D.** and **C.D.** synthesized the materials. **A.Q.** designed the sample holder to carry out magnetometry under voltage application (*i.e.*, magnetoelectric measurements). **J.d.R.**, **J.S.** and **E.M.** carried out the magnetoelectric measurements and analyzed the data.

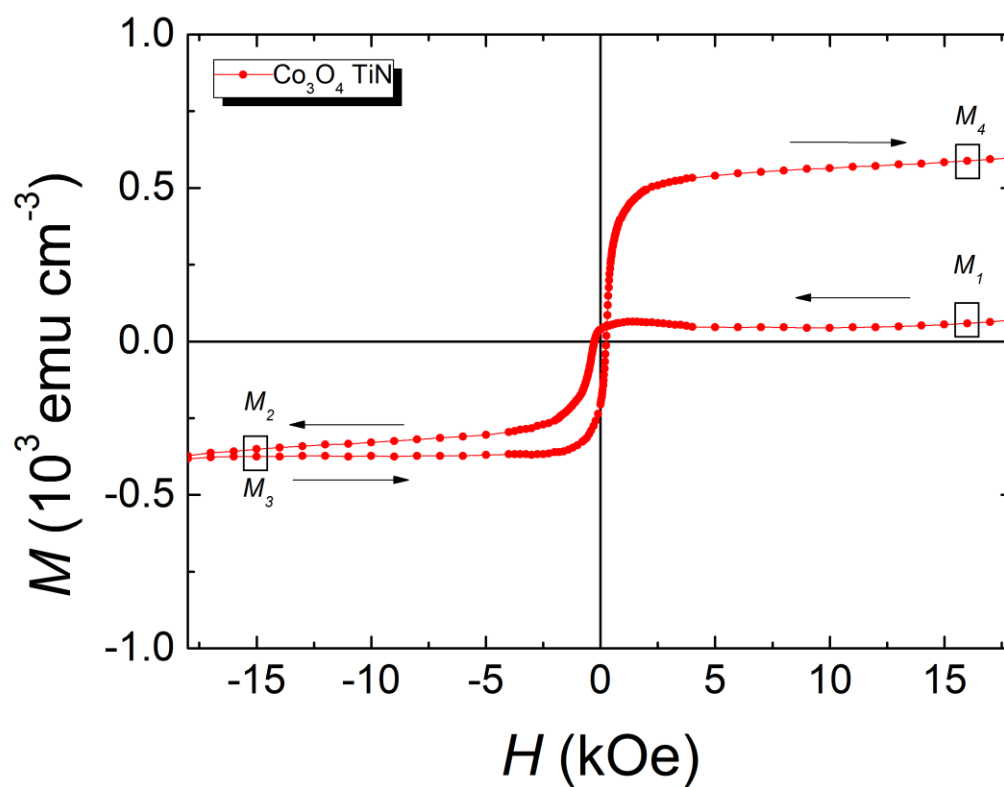
J.d.R., A.Q. and **E.M.** performed the XRD and TEM characterization and analyzed the corresponding data. **A.L.** and **L.A.** conducted the COMSOL simulations. **J.S., B.M.** and **J.L.C.** performed the electrical characterization of the samples. **M.O.L., M.B.** and **A.W.** characterized the samples by VEPAS and analyzed the data. All authors discussed the results and commented on the article. The article was written by **J.d.R., J.S.** and **E.M.**

Competing financial interests

The authors declare no competing financial interests.

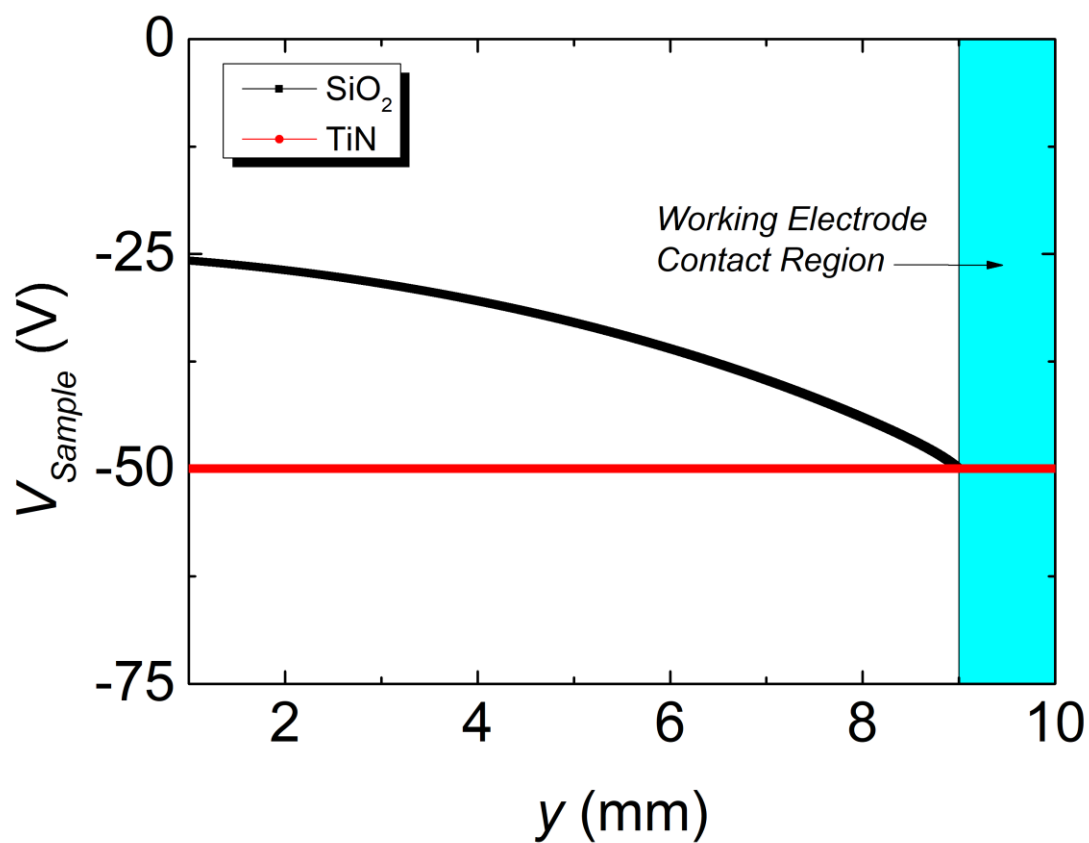
Supplementary Information

Supplementary Figure 1



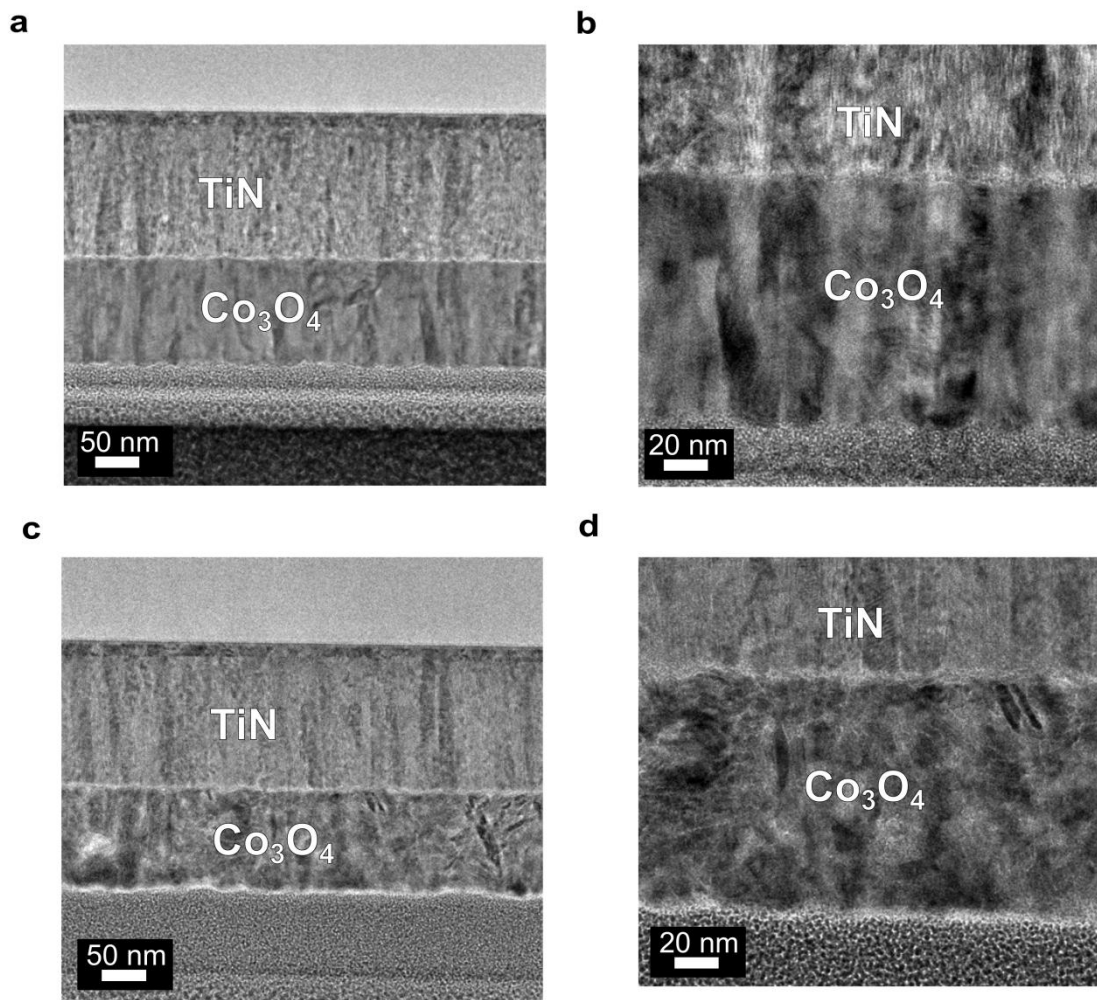
Saturation magnetization (M_s) from hysteresis loops. The cartoon is based on the first hysteresis loop of the Co_3O_4 film grown on TiN (conducting configuration) upon electrolyte-gating at -50 V. Since sample magnetization is continuously evolving, the M_s is taken at ± 15 kOe for each of the quadrants of the hysteresis loop (*i.e.*, M_1 , M_2 , M_3 and M_4).

Supplementary Figure 2



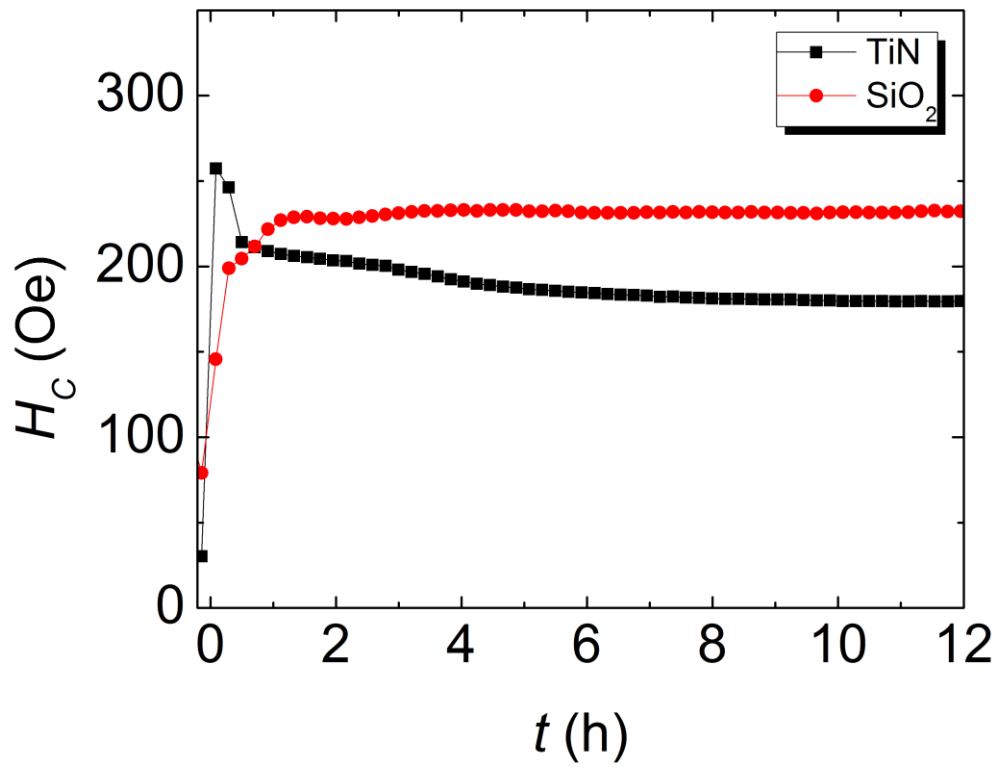
Electric potential (upon electrolyte-gating at -50 V) at the bottom of the Co_3O_4 layer along the length of the sample for both configurations: Co_3O_4 on either SiO_2 (insulating) or TiN (conducting).

Supplementary Figure 3



(a) and (b) are transmission electron microscopy (TEM) images of the cross-section of an as-prepared Co₃O₄ film grown on TiN, and (c) and (d) are TEM images corresponding to the same sample but treated at -50 V for 80 min.

Supplementary Figure 4



Coercive field (H_c) evolution with time for Co_3O_4 films grown on either SiO_2 (insulating configuration) or TiN (conducting configuration) subjected to a voltage of -50 V for several hours.